High thermoelectric and mechanical performance in the n-type polycrystalline SnSe incorporated with multi-walled carbon nanotubes

Xin-Yu Mao[1,†], *Xiao-Lei Shi*[2,3,†], *Liang-Chuang Zhai*[1], *Wei-Di Liu*[4], *Yue-Xing Chen*[5], *Han Gao*[6], *Meng Li*[7], *De-Zhuang Wang*[1], *Hao Wu*[1], *Zhuang-Hao Zheng*[5], *Yi-Feng Wang*[8,9], *Qingfeng Liu*[1,10,*], *Zhi-Gang Chen*[2,3,*]

[1] State Key Laboratory of Materials-Oriented Chemical Engineering, College of Chemical Engineering, Nanjing Tech University, Nanjing 211816, China.

[2] Centre for Future Materials, University of Southern Queensland, Springfield Central, Brisbane, Queensland 4300, Australia.

[3] School of Chemistry and Physics, Queensland University of Technology, Brisbane, Queensland 4000, Australia.

[4] Australian Institute for Bioengineering and Nanotechnology, The University of Queensland, Brisbane, QLD 4072, Australia.

[5] Shenzhen Key Laboratory of Advanced Thin Films and Applications, Key Laboratory of Optoelectronic Devices and Systems of Ministry of Education and Guangdong Province, College of Physics and Optoelectronic Engineering, Shenzhen University, Shenzhen 518060, China.

[6] Key Laboratory of Material Physics of Ministry of Education, School of Physics and Microelectronics, Zhengzhou University, Zhengzhou 450052, China.

[7] School of Mechanical and Mining Engineering, The University of Queensland, St Lucia, Brisbane, Queensland 4072, Australia.

[8] College of Materials Science and Engineering, Nanjing Tech University, Nanjing 211816, China.

[9] Jiangsu Collaborative Innovation Center for Advanced Inorganic Function Composites, Nanjing Tech University, Nanjing 211816, China.

[10] CAS Key Laboratory of Carbon Materials, Institute of Coal Chemistry, Chinese Academy of Sciences, Taiyuan 030001, China.

† These authors contribute equally to this work.

* Corresponding authors:

Qingfeng Liu: qfliu@njtech.edu.cn;

Zhi-Gang Chen: zhigang.chen@usq.edu.au, zhigang.chen@uq.edu.au.

Abstract:

In this study, we introduce multi-walled carbon nanotubes (MWCNTs) in Pb/I co-doped n-type polycrystal SnSe to simultaneously improve its thermoelectric and mechanical properties for the first time. The introduced MWCNTs act as the "bridges" to accelerate the electron carrier transport between SnSe grains, leading to significantly increased electrical conductivity from 32.6 to 45.7 S cm^{-1} at 773 K, which contributes to an enhanced power factor of ~5.0 μW cm^{-1} K^{-2} at this temperature. Although MWCNTs possess high intrinsic thermal conductivities, these MWCNTs, acting as nanoinclusions in the SnSe matrix to form the dense interfaces between SnSe and MWCNTs, provide extra heat-carrying phonon scattering centers, leading to a slightly reduced lattice thermal conductivity of only 0.34 W m^{-1} K^{-2} at 773 K and in turn, a high *ZT* of ~1.0 at this temperature. Furthermore, the introduced MWCNTs can simultaneously act as the "binders" to bond adjacent grains, significantly improving the mechanical properties of SnSe by boosting its Vickers hardness from 39.5 to 50.5. This work indicates that our facile approach can achieve high thermoelectric and mechanical properties in n-type SnSe polycrystals with a considerable potential for applying to thermoelectric devices as n-type elements.

Keywords: thermoelectric; SnSe; n-type; multi-walled carbon nanotubes; mechanical.

1. Introduction

Thermoelectrics has been treated as a unique technology to tackle the upcoming crisis in energy-depleting and environmental pollution by enabling the direct conversion between heat and electricity [1]. To increase the thermoelectric conversion efficiency of the thermoelectric devices, materials used in the devices must possess high thermoelectric performance, which can be evaluated by the dimensionless figure-of-merit ZT, defined as $ZT = (S^2\sigma/\kappa)/T$ [2, 3], where S, σ, κ, and T are the Seebeck coefficient, the electrical conductivity, the thermal conductivity, and the absolute temperature, respectively. Here $S^2\sigma$ can be described as the thermoelectric power factor, while κ is contributed by the electronic thermal conductivity κ_e and the lattice thermal conductivity κ_l [4, 5]. Both high $S^2\sigma$ and low κ can induce high ZT. Historically, doping or alloying with other elements or compounds is widely employed to tune the carrier concentration n (n_e for electrons as the major carriers and n_p for holes as the major carriers) and in turn, to optimize $S^2\sigma$ [6], while hierarchical nano/microstructural structures are designed to suppress κ_l since κ_l is not strongly related to n [1]. Furthermore, to ensure a stable power output of the devices, the thermoelectric materials mainly need to be mechanical robust enough to resist external force such as physical shock and pressure [6].

With advances in the field of thermoelectrics, various advanced inorganic thermoelectric materials with high performance have been reported with a peak ZT of >2, such as PbTe with a ZT of ~2.5 at 823 K [7], GeTe with a ZT of ~2.4 at 600 K [8], $Cu_{2-x}Se$ with a ZT of ~2.7 at 973 K [9], $AgSbTe_2$ with a ZT of ~2.1 at 573 K [10], and SnSe with a ZT of ~3.1 at 783 K [11]. Among these state-of-the-art thermoelectric materials, SnSe shows ultrahigh ZT [12], derived from its unique electrical transport behaviors and ultralow intrinsic κ_l [13], and has achieved great attention. SnSe is a typical semiconductor with low-toxic, easy-fabrication, and cost-effective features [13]. Single-crystal SnSe bulk materials were reported to exhibit high peak and average ZT values, such as p-type $Sn_{0.91}Pb_{0.09}Se$ crystal with an average ZT of 1.9 [14] and n-type Br-doped SnSe crystal with a peak ZT of 2.8 at 773 K [12]. Compared with single-crystal SnSe, polycrystalline SnSe is also promising to be employed in

devices due to the high cost of fabricating SnSe crystals as well as their easy-crack features from their layered crystal structures (see **Figure S1** in the Supporting Information). P-type polycrystalline SnSe was reported to have an outstanding *ZT* of ~3.1 at 783 K [11], derived from the Na-doping and the unique oxide-removal technique; while other works also reported p-type polycrystalline SnSe with high peak *ZT*s of >2.2 by co-alloying with CdSe [15], doping with Ge [16], co-alloying with PbSe and Na [17], and co-doping with Zn and Pb [18]. However, a highly efficient thermoelectric device requires both n-type and p-type thermoelectric materials with a similar thermoelectric system [6]. Therefore, developing n-type polycrystalline SnSe with high performance is of significance.

Historically, realizing high *ZT* in n-type SnSe polycrystals is tricky due to the existence of Sn vacancies in native pure SnSe, which is the main reason for the p-type nature of SnSe [19]. Generally, doping/alloying with halogens such as Br and I to substitute the Se sites [12, 20], as well as doping/alloying with V-A group elements such as Bi and Sb to substitute the Sn sites [21, 22], were commonly used to realize the n-type doping in SnSe, while boosting the density of Se vacancy is also an effective strategy to achieve this goal [23]. Both conventional melting and aqueous solution methods can realize the above doping [24]. By employing rational doping/alloying and micro/nanostructure manipulations, *ZT* values of n-type polycrystalline SnSe can be significantly improved from nearly zero to ~1.7 at 793 K [23, 25-28]. However, the doping and alloying with other elements or compounds also severely damage the mechanical properties of n-type polycrystalline SnSe, making it easy to crack or be difficult to resist high temperatures [6]. In this situation, it is highly needed to explore an effective way to improve the mechanical properties of n-type polycrystalline SnSe while maintaining its thermoelectric performance. Historically, vacancy engineering was proved to be effective in strengthening the mechanical properties of polycrystalline SnSe by vacancy-induced dispersion strengthen [29], but it is tricky to control the Se vacancy in n-type SnSe due to its high formation energy [30]. A combustion process was reported to inhibit the grain growth of polycrystalline SnSe by introducing the pre-synthesized SnSe that promotes multipoint nucleation

[31], but it is difficult to realize a fine composition control by such a route towards high-performing n-type doping.

To tackle this issue, in this work, we introduce multi-walled carbon nanotubes (MWCNTs) in the n-type Pb/I co-doped polycrystal SnSe to simultaneously improve its thermoelectric and mechanical properties by a conventional melting route combined with a sparkle plasma sintering technique, as illustrated by **Figure 1(a)**. Here, Pb and I act as n-type dopants to transfer the p-type SnSe into n-type with an optimized *ZT* of 0.79 at 773 K (refer to **Figure S2**). Furthermore, the MWCNTs are introduced to act as the "bridges" to accelerate the electron carrier transport between adjacent SnSe grains, contributing to an improved σ from 32.6 to 45.7 S cm^{-1} and in turn, an enhanced $S^2\sigma$ of ~5.0 μW cm^{-1} K^{-2} at 773 K. Meanwhile, the MWCNTs act as nanoinclusions in the SnSe matrix as shown in **Figure 1(b)**, providing extra phonon scattering centers such as the dense interfaces between SnSe and MWCNTs, leading to a low κ_l of ~0.34 W m^{-1} K^{-2} and a competitive *ZT* of ~1.0 at 773 K, as shown in **Figure 1(c)**. Besides, the introduced MWCNTs can simultaneously act as the "binders" to bond adjacent SnSe grains by strengthening their adhesive forces, significantly improving the Vickers hardness of SnSe from 39.5 to 50.5, as shown in **Figure 1(d)**. The Vickers hardness of sample the was randomly performed on a polished surface at 10 different areas at room temperature. The mechanical strengthening by CNTs was also proved to be potentially effective in Bi_2Te_3-based thermoelectric materials [32]. Such a high-performing and mechanical robust n-type polycrystalline SnSe is promising for practical applications as n-type elements in thermoelectric devices.

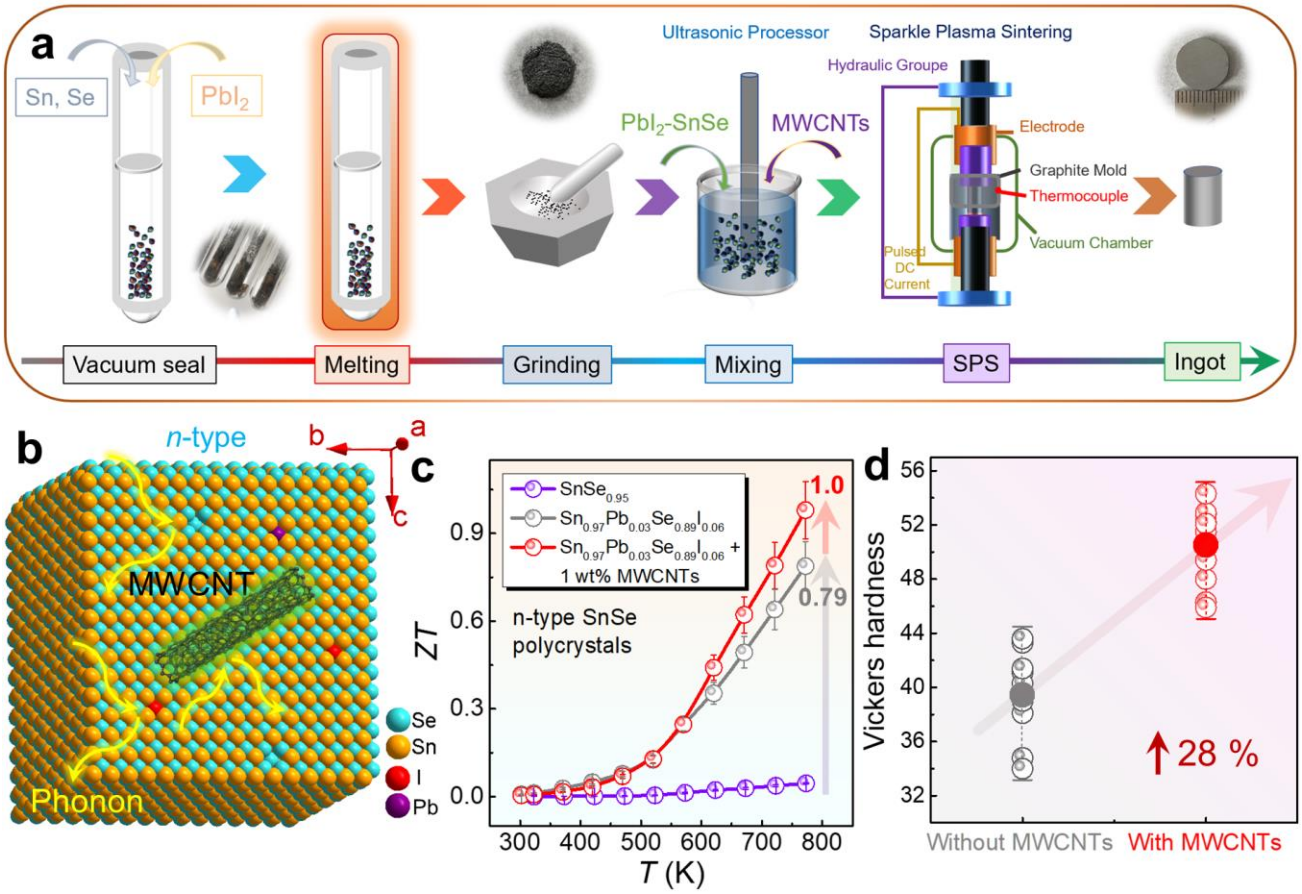

Figure 1. (a) Schematic diagram of fabricating PbI_2-doped polycrystalline SnSe incorporated with MWCNTs. (b) Illustration of the crystal structure of PbI_2-doped SnSe incorporated with MWCNTs. (c) Comparison of temperature-dependent *ZT* of $SnSe_{0.95}$, $Sn_{0.97}Pb_{0.03}Se_{0.89}I_{0.06}$, and $Sn_{0.97}Pb_{0.03}Se_{0.89}I_{0.06}$ + 1 wt% MWCNTs. (d) Vickers hardness of PbI_2-doped SnSe with and without MWCNTs.

2. Results and Discussions

In this study, we use 3 % PbI_2-doped SnSe as a base material to study the effects of MWCNTs on n-type polycrystalline SnSe (abbreviated as n-SnSe) because 3 % PbI_2 is a well-tuned doping concentration to optimize the *ZT* of n-SnSe up to 0.79 at 773 K (see **Figure S2**), and iodine acts as the dopant to transfer the p-type into the n-type by shifting the Fermi level into the conduction band in SnSe (see **Figure S3**). Here, we choose different contents of MWCNTs to investigate their effects on the thermoelectric properties of SnSe, including 0.5 wt%, 1 wt%, and 2 wt%. To investigate the phases

of the as-fabricated n-SnSe pellets incorporated with different contents of MWCNTs, their X-ray diffraction (XRD) patterns were investigated, and the results are shown in **Figure 2(a)**. All peaks from all samples can be fully indexed as room-temperature orthorhombic SnSe according to PDF#48-1224. The strongest peak for all samples is (400) peak, indicating a strong anisotropy in the pellets, derived from the layered structure of SnSe (see **Figure S1**). As well, XRD is difficult to index the MWCNT phase due to its detection limit [33]. Therefore, we further employed Raman spectroscopy to analyze n-SnSe incorporated with MWCNTs, and the results are shown in **Figure 2(b)**. The peaks at <250 cm^{-1} belong to the SnSe phase (here the peaks at 58 cm^{-1} , 69 cm^{-1}, 107 cm^{-1}, and 167 cm^{-1} refer to the B1g vibration mode, the A1g vibration mode, the B3g vibration mode, and the A3g vibration mode, respectively) [34], while the two peaks at ~1350 cm^{-1} and ~1590 cm^{-1} belong to the D mode and G mode of the MWCNTs, respectively [35]. With increasing the MWCNT content, the intensities of these two peaks are increased. These results confirm the successful incorporation of MWCNTs in the SnSe matrix.

To understand the morphological features of the as-fabricated n-SnSe incorporated with MWCNTs, scanning electronic microscopy (SEM) was investigated. **Figure 2(c)** displays a typical SEM image of the cracked n-SnSe incorporated with 1 wt% MWCNTs, from which a typical polycrystalline feature with layered grains can be observed. Such a layered feature indicates a potential anisotropy in their thermoelectric properties. **Figure 2(d)** shows a typical SEM image of a grain of the n-SnSe. This grain exhibits a layered structure, derived from its layered Sn-Se chains stacked layer-by-layer along the out-of-plane direction. Sometimes micro-sized pores can be occasionally found in the grains, as shown in **Figures 2(e-f)**, which is a common phenomenon in SnSe polycrystals fabricated by the melting route [13]. These micropores can contribute to low κ since the surfaces of the pores can absolutely scatter all phonons [36], but may potentially reduce the mass density of the materials (see **Table S1** in the Supporting Information). **Figure 2(g)** is a SEM image of the cracked n-SnSe with MWCNTs and shows general morphologies of the incorporated MWCNTs. As can be seen, the

MWCNTs are mainly at the grain boundaries of adjacent SnSe grains. **Figure 2(h)** is a magnified SEM image of MWCNTs on the surface of one n-SnSe grain, and **Figure 2(i)** is another magnified SEM image of MWCNTs linked between two n-SnSe grains. As can be seen, MWCNTs connect adjacent SnSe grains, accounting for the enhanced σ and mechanical properties.

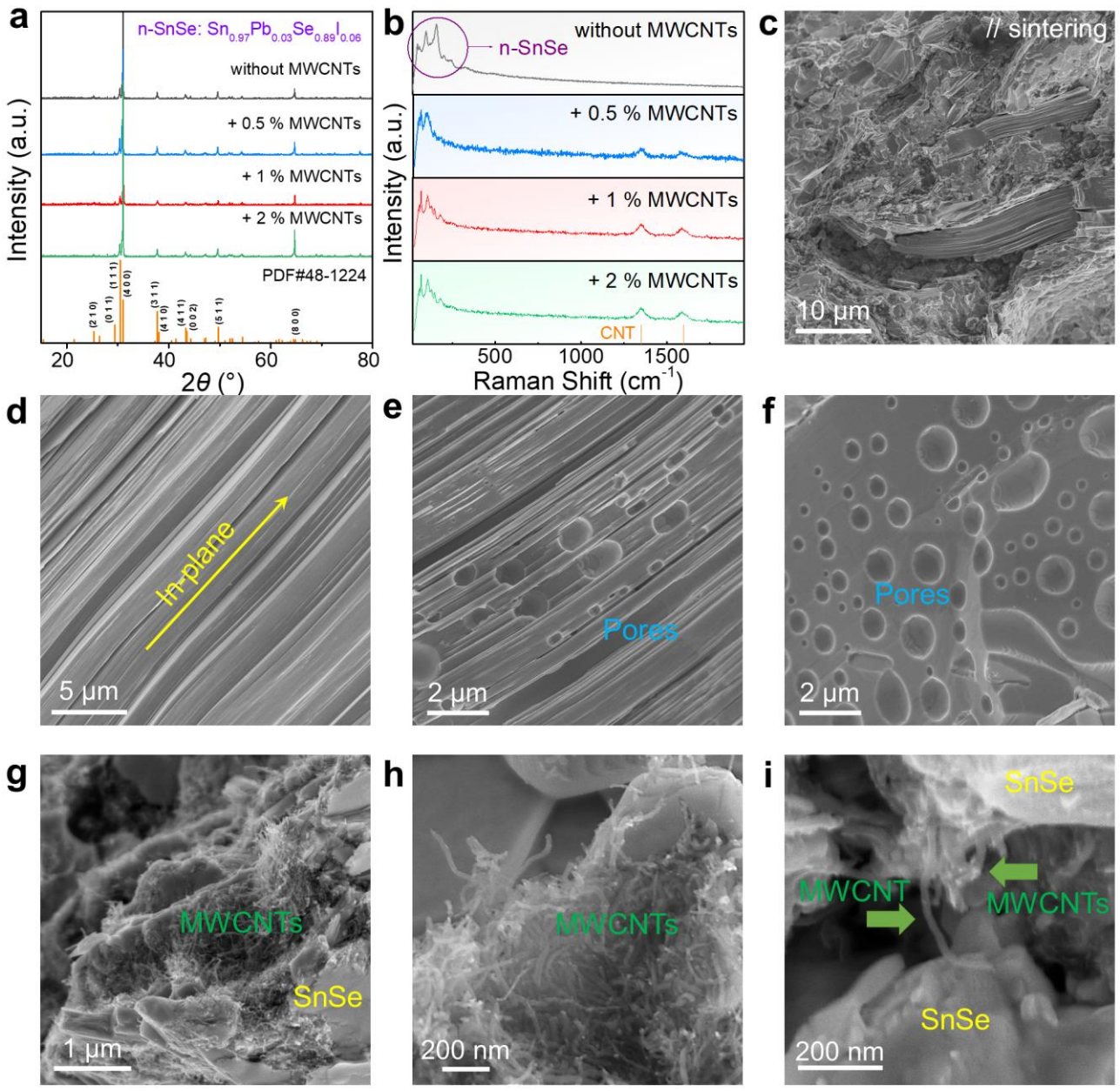

Figure 2. (a) XRD and (b) Raman spectrums of 3% PbI_2-doped polycrystalline n-SnSe incorporated with different contents of MWCNTs. (c) Scanning electronic microscopy (SEM) image of cracked n-SnSe incorporated with 1 wt% MWCNTs. (d) SEM image of a typical n-SnSe grain with a layered structure. SEM images of micropores found in n-SnSe grains viewed from the (e) in-plane and (f) out-

of-plane directions. (g) SEM image of cracked n-SnSe with MWCNTs. (h) Magnified SEM image of MWCNTs on the surface of one n-SnSe grain. (i) Magnified SEM image of MWCNTs linked between two n-SnSe grains.

To investigate the micro/nanostructure characteristics of n-SnSe incorporated with MWCNTs, transmission electron microscopy (TEM) and spherical aberration-corrected scanning transmission electron microscopy (Cs-STEM) were investigated. **Figure 3(a)** shows a Cs-STEM high-angle annular dark-field (HAADF) image of n-SnSe prepared by the focused ion beam (FIB) technique. As can be seen, dense grain boundaries can be observed. **Figure 3(b)** is corresponding energy dispersive spectroscopy (EDS) maps of Sn, Se, Pb, and I. All elements are uniformly distributed, indicating a uniform composition in the as-fabricated pellet. **Figure 3(c)** is a STEM image of the n-SnSe matrix and the observed contrast different from the matrix shows nanoprecipitates exited. These nanoprecipitates were commonly found in doped SnSe fabricated by melting route [13]. **Figure 3(d)** shows a TEM image of the contrast interface between the n-SnSe matrix and the nanoprecipitate, from which no obvious difference in the lattice structure can be found between the SnSe matrix and the nanoprecipitate. **Figure 3(e)** also shows the corresponding selected area electron diffraction (SAED) pattern taken from **Figure 3(d)**. No extra SAED pattern can be found from **Figure 3(e)**, indicating that the as-observed potential "nanoprecipitates" are in fact SnSe with slight differences in zone axis from the SnSe matrix. **Figure 3(f)** shows a high-resolution TEM (HRTEM) image of the n-SnSe matrix, indicating a typical crystal feature with no obvious lattice imperfections, indicating that Pb and I are uniformly doped. In terms of the MWCNTs incorporated into the SnSe matrix, **Figure 3(g)** shows a HRTEM image of the interfaces between the n-SnSe matrix and MWCNTs, from which the MWCNTs possess typical multi-walled features, and the interfaces between the n-SnSe matrix and the MWCNTs are clearly shown. These interfaces are dense, and there is no crack between the n-SnSe matrix and the MWCNTs, indicating good adhesion between the n-SnSe matrix and MWCNTs. Such a phenomenon

will benefit a high electrical transport performance. **Figure 3(h)** shows the corresponding SAED pattern taken from **Figure 3(g)**, from which multiple patterns can be observed due to the overlap of the n-SnSe matrix and MWCNTs. All these results confirm the co-existence of the n-SnSe matrix and MWCNTs with good combinations. More TEM evidence can be referred to **Figure S4**. Based on these crystal and lattice imperfections, **Figure 3(i)** shows calculated spectral lattice thermal conductivity (κ_s) of n-SnSe with 1 wt% MWCNTs at 300 K using the Debye-Callaway model (see **Table S2** for detailed parameters). Benefited from the point defects by Pb/I-doping and nanoinclusions by incorporating MWCNTs, ultralow κ can be expected in the as-fabricated n-SnSe.

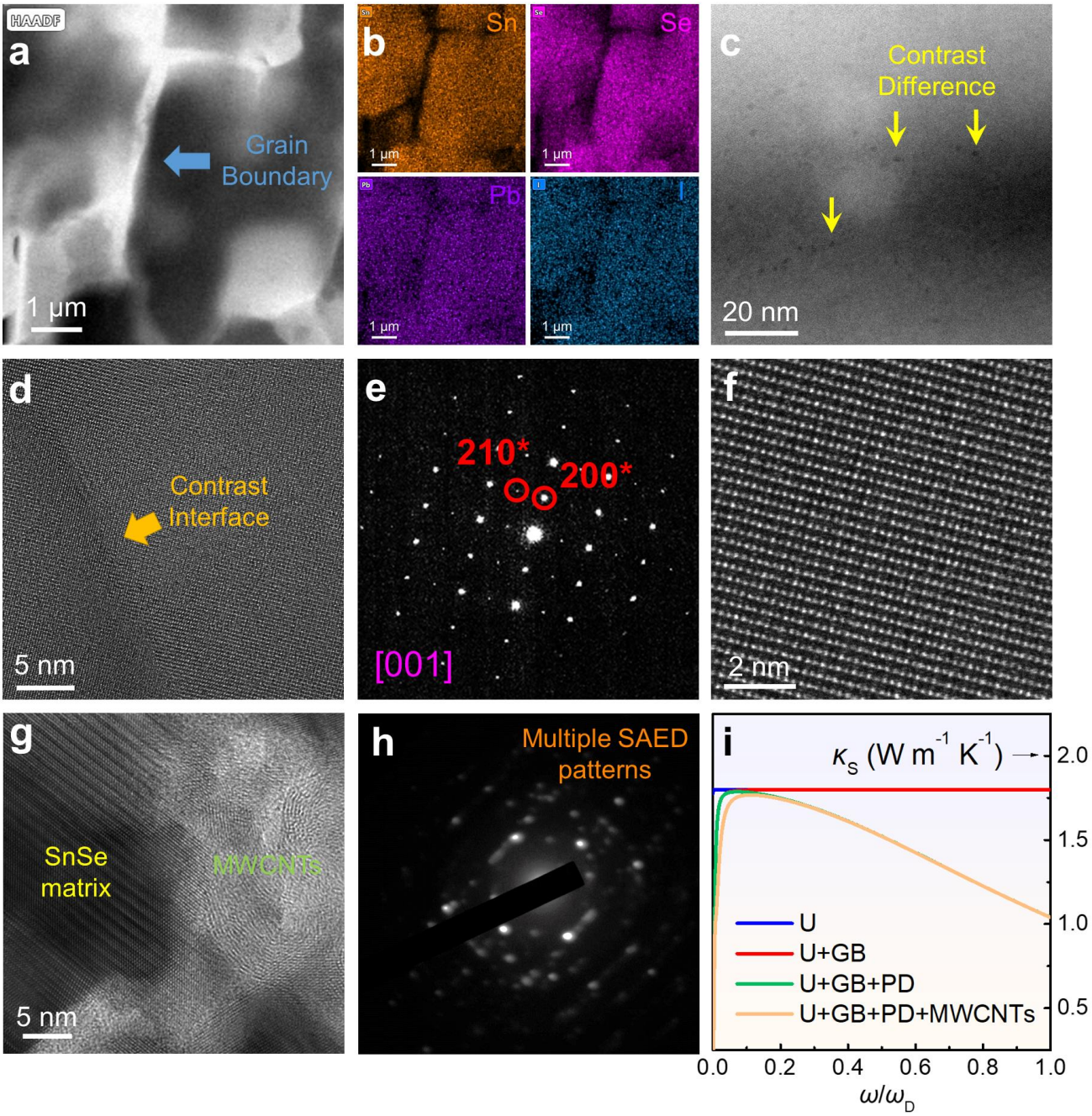

Figure 3. (a) Spherical aberration-corrected scanning transmission electron microscopy (Cs-STEM) high-angle annular dark-field (HAADF) image of n-SnSe to show grain boundaries. (b) Corresponding energy dispersive spectroscopy (EDS) maps of Sn, Se, Pb, and I. (c) STEM image of the n-SnSe matrix to show some nanoprecipitates with different contrast from the matrix. (d) TEM image of the contrast interface between n-SnSe matrix and nanoprecipitate. (e) Corresponding selected area electron diffraction (SAED) pattern of (d). (f) High-resolution TEM (HRTEM) image of n-SnSe matrix. (g) HRTEM image of the interfaces between n-SnSe matrix and MWCNT. (h) Corresponding SAED

pattern of (g). (i) Calculated spectral lattice thermal conductivity (κ_s) of n-SnSe with 1 wt% MWCNTs at 300 K using the Debye-Callaway model.

To evaluate the effects of MWCNTs on thermoelectric properties of n-SnSe, temperature-dependent σ, S, and $S^2\sigma$ of n-SnSe incorporated with MWCNTs were evaluated from 300 K to 773 K. All data were measured along the direction perpendicular to the sintering pressure. **Figure 4(a)** plots temperature-dependent σ of the n-SnSe incorporated with MWCNTs. With increasing the content of MWCNTs from 0 to 1 wt%, the σ is significantly enhanced, especially at high temperatures of >500 K. However, when the MWCNT content is at 2 wt%, although the σ is obviously enhanced at low temperature due to the potentially enhanced n_e by introducing MWCNTs, the σ value is significantly reduced at high temperatures of >500 K, which may be derived from the carrier scattering at the dense boundaries between MWCNTs and SnSe matrix because electron carriers can be thermally excited and strengthen the scattering at high temperature. Therefore, the excessive MWCNTs may reduce the σ at high temperatures. **Figure 4(b)** compares temperature-dependent S. Introducing MWCNTs potentially enhances the n_e due to the n-type nature of MWCNTs, leading to reduced S potentially. Nevertheless, after introducing 1 wt% MWCNTs, the $S^2\sigma$ is still retained up to ~5.0 μW cm^{-1} K^{-2} at 773, coming from the coupling of significantly enhanced σ and slightly reduced S, as shown in **Figure 4(c)**.

To further understand the fundamental physics in the as-achieved electrical transport properties of n-SnSe incorporated with MWCNTs, **Figure 4(d)** shows the n_e and mobility μ as a function of MWCNTs content. With the rise of the MWCNT content from 0 to 1 wt%, the n_e is only slightly increased. However, when the MWCNTs content is increased up to 2 wt%, there is an obvious increase in the n_e, explaining the increased σ. The increased n_e should come from the increased MWCNT content since MWCNT shows a typical n-type electronic transport behavior in many cases [37]. The μ is much fluctuated after introducing the MWCNTs, which may be caused by the interactions between carriers and interfaces between the MWCNTs and the SnSe matrix. **Figure 4(e)** shows the calculated

effective mass m^*, calculated by a single parabolic band (SPB) model. When the MWCNT content is 1 wt%, the lowest m^* indicates the lowest low-energy carrier scattering. In other words, this result confirms the function of MWCNTs that act as "bridges" to facilitate the electron carrier transport rather than filter or scatter the carriers as interfaces, and also explains the slight reduction in the as-achieved S. **Figure 4(f)** plots calculated n_e-dependent $S^2\sigma$ of the n-SnSe incorporated with MWNTs from the SPB model and shows higher $S^2\sigma$ can be achieved by further tuning the n_e toward a higher value.

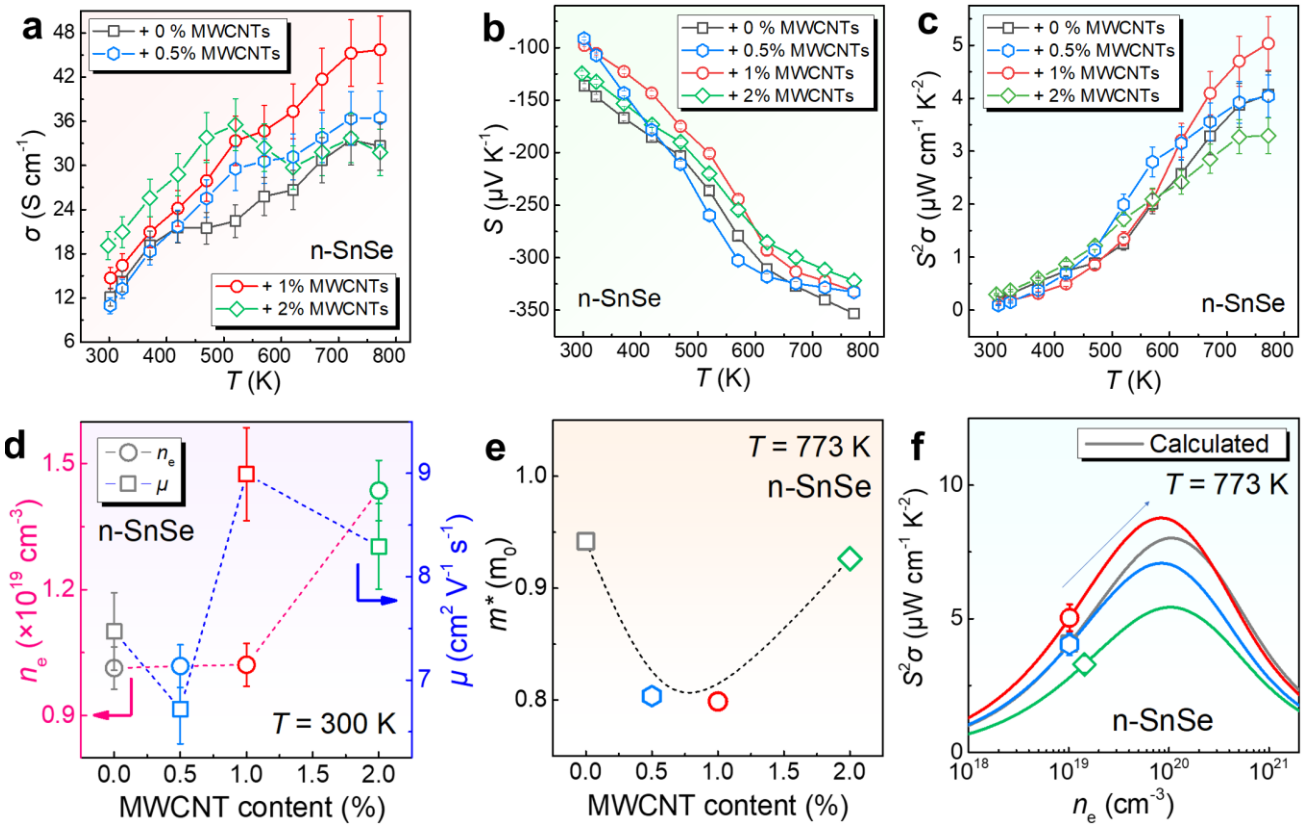

Figure 4. T-dependent (a) electrical conductivity σ, (b) Seebeck coefficient S, and (c) power factor $S^2\sigma$ of the n-SnSe incorporated with MWCNTs. (d) Electron carrier concentration n_e and mobility μ, (e) effective mass m^*, and (f) n_e-dependent $S^2\sigma$ of n-SnSe incorporated with MWCNTs. All properties are measured or determined along the direction perpendicular to the sintering pressure.

In terms of the thermal transport performance of n-SnSe incorporated with different contents of MWCNTs, we further plotted temperature-dependent κ of the n-SnSe incorporated with MWCNTs along the direction perpendicular to the sintering pressure in **Figure 5(a)**. After incorporating the

MWCNTs, κ is slightly increased due to the high κ of MWCNTs (2000-6000 W m^{-1} K^{-1} [38]). **Figure 5(b)** displays temperature-dependent κ_e of the n-SnSe incorporated with MWCNTs, calculated according to the Wiedemann-Franz law as $\kappa_e = L\sigma T$ [6], where the Lorenz number L is calculated (refer to **Figure S5**). The κ_e possesses the same trends of σ but with very low values, indicating that the κ_l dominate the κ. **Figure 5(c)** shows temperature-dependent κ_l of the n-SnSe incorporated with MWCNTs by $\kappa_l = \kappa - \kappa_e$. After incorporating MWCNTs up to 1 wt%, the κ_l can be slightly reduced to only 0.34 W m^{-1} K^{-2} at 773 K. This is because these MWCNTs act as nanoinclusions in the matrix of SnSe, providing extra heat-carrying phonon scattering centers such as the dense interfaces between SnSe and MWCNTs. **Figure 5(d)** plots the 1000/T-dependent κ_l, from which linear relationship can be observed for all the plots, indicating that the phonon scattering is dominated by the Umklapp phonon scattering [19, 23, 39, 40]. **Figure 5(e)** shows determined temperature-dependent ZT, from which a high ZT of ~1.0 can be achieved at 773 K by introducing 1 wt% MWCNTs in n-SnSe. Such a high ZT is competitive compared with the reported values (see **Table S3**), and the mechanical robust feature makes it be a promising candidate to be employed in practical thermoelectric devices as the n-type element. **Figure 5(f)** shows calculated n_e-dependent ZT of the n-SnSe incorporated with MWCNTs, from which higher ZT can be achieved by further tuning the n_e toward a higher value, indicating the room for future improvement. In terms of the determination of error bars, the repeatability is achieved with measured fluctuations of σ, S, and κ being 10%, 2%, and 5%, respectively, and the combined uncertainty for the experimental determination of ZT is about 15%–20%.

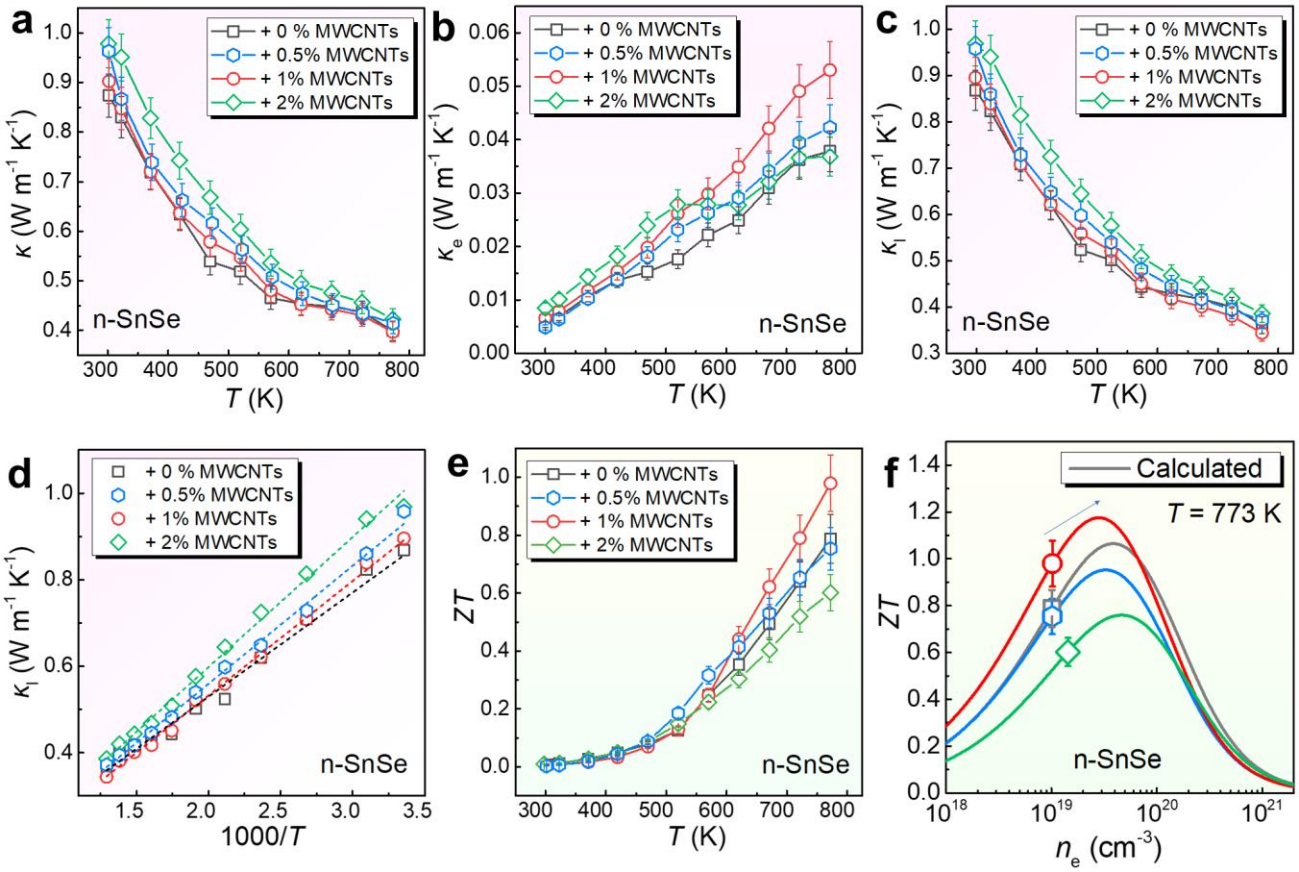

Figure 5. *T*-dependent (a) thermal conductivity κ, (b) electronic thermal conductivity κ_e, and (c) lattice thermal conductivity κ_l of n-SnSe incorporated with different contents of MWCNTs. (d) 1000/*T*-dependent κ_l, (e) *T*-dependent *ZT*, and (f) n_e-dependent *ZT* of n-SnSe incorporated with different contents of MWCNTs. All properties are measured or determined along the direction perpendicular to the sintering pressure.

It should be noted that higher peak *ZT* and average *ZT* values are still required for n-type SnSe to ensure a high power density when employing these n-type SnSe-based thermoelectric materials into the practical devices that work within a wide temperature range. As well, high mechanical properties are needed to strengthen the stability of the devices. To achieve these goals, a rationally tuned n_e as well as a well-designed micro/nanostructure are both needed. Exploring suitable n-type doping or alloying materials is a suitable way to finely tune the n_e, while exploring potential effective nanoinclusions can strengthen the mechanical performance, but such nanoinclusions should not

damage the thermoelectric properties. Therefore, combination routes should be considered when designing high-performing and mechanical robust n-type thermoelectric materials in the future [6].

3. Conclusion

In this work, a novel n-type polycrystalline SnSe incorporated with MWCNTs show both high thermoelectric performance and high mechanical property. MWCNTs play mainly three functions in the as-achieved hybrid materials, namely (i) acting as the "bridges" to accelerate the electron carrier transport between SnSe grains and lead to significantly increased electrical conductivity and power factor of ~5.0 μW cm^{-1} K^{-2} at 773 K; (ii) acting as phonon scattering centers to provide dense interfaces between SnSe and MWCNTs, leading to a slightly reduced lattice thermal conductivity of 0.34 W m^{-1} K^{-2} at 773 K and a high *ZT* of ~1.0 at this temperature; and (iii) acting as the "binders" to bond adjacent SnSe grains, significantly boosting the Vickers hardness from 39.5 to 50.5. This work indicates a simple way to simultaneously realize high thermoelectric and mechanical performance in n-type polycrystalline SnSe with considerable potential for practical applications.

4. Experimental

The experimental details can be referred in Supporting Information.

Author contributions

Z.G.C and Q.F.L. lead the project. X.L.S. and X.Y.M. draft the original manuscript. Z.G.C., Q.F.L., and Y.F.W. revise the manuscript. X.Y.M., X.L.S., Q.F.L., and Z.G.C. design the experiments; X.Y.M. and Y.X.C. perform the material synthesis and sample measurement; W.D.L. and M.L. perform the theoretical calculation; Y.X.C., H.G., and Z.H.Z. conduct the SEM and TEM characterizations. D.Z.W., H.W., and L.C.Z. conduct the Raman and XRD characterizations. Everyone was involved in writing the article.

Conflicts of interest

The authors declare no competing financial interest.

Declaration of competing interest

The authors declare that they have no known competing financial interests or personal relationships that could have appeared to influence the work reported in this paper.

Acknowledgements

This work was financially supported by the National Natural Science Foundation of China (No. 51972170), the State Key Laboratory of Materials-Oriented Chemical Engineering (No. ZK201812), the CAS Key Laboratory of Carbon Materials (No. KLCMKFJJ2002), the Priority Academic Program Development of Jiangsu Higher Education Institutions (PAPD), the Jiangsu Specially-Appointed Professor Program. ZGC thanks the financially support from the Australian Research Council, Innovation Centre for Sustainable Steel (ICSS), and USQ strategic research grant.

Reference

[1] Y. Zheng, T.J. Slade, L. Hu, X.Y. Tan, Y. Luo, Z.-Z. Luo, J. Xu, Q. Yan, and M.G. Kanatzidis, Chem. Soc. Rev. 50 (2021) 9022-9054.

[2] S. Roychowdhury, T. Ghosh, R. Arora, M. Samanta, L. Xie, N.K. Singh, A. Soni, J. He, U.V. Waghmare, and K. Biswas, Science 371 (2021) 722.

[3] B. Jiang, Y. Yu, J. Cui, X. Liu, L. Xie, J. Liao, Q. Zhang, Y. Huang, S. Ning, B. Jia, B. Zhu, S. Bai, L. Chen, S.J. Pennycook, and J. He, Science 371 (2021) 830.

[4] Y. Xiao and L.-D. Zhao, Science 367 (2020) 1196.

[5] X. Shi and L. Chen, Nat. Mater. 15 (2016) 691-692.

[6] X.-L. Shi, J. Zou, and Z.-G. Chen, Chem. Rev. 120 (2020) 7399-7515.

[7] Y. Wu, Z. Chen, P. Nan, F. Xiong, S. Lin, X. Zhang, Y. Chen, L. Chen, B. Ge, and Y. Pei, Joule 3 (2019) 1276-1288.

[8] X. Zhang, Z. Bu, S. Lin, Z. Chen, W. Li, and Y. Pei, Joule 4 (2020) 986-1003.

[9] D. Yang, X. Su, J. Li, H. Bai, S. Wang, Z. Li, H. Tang, K. Tang, T. Luo, Y. Yan, J. Wu, J. Yang, Q. Zhang, C. Uher, M.G. Kanatzidis, and X. Tang, Adv. Mater. 32 (2020) 2003730.

[10] M. Hong, Z.G. Chen, L. Yang, Z.M. Liao, Y.C. Zou, Y.H. Chen, S. Matsumura, and J. Zou, Adv. Energy Mater. 8 (2017) 1702333.

[11] C. Zhou, Y.K. Lee, Y. Yu, S. Byun, Z.-Z. Luo, H. Lee, B. Ge, Y.-L. Lee, X. Chen, J.Y. Lee, O. Cojocaru-Mirédin, H. Chang, J. Im, S.-P. Cho, M. Wuttig, V.P. Dravid, M.G. Kanatzidis, and I. Chung, Nat. Mater. 20 (2021) 1378-1384.

[12] C. Chang, M. Wu, D. He, Y. Pei, C.-F. Wu, X. Wu, H. Yu, F. Zhu, K. Wang, and Y. Chen, Science 360 (2018) 778-783.

[13] Z.-G. Chen, X. Shi, L.-D. Zhao, and J. Zou, Prog. Mater. Sci. 97 (2018) 283-346.

[14] B. Qin, D. Wang, X. Liu, Y. Qin, J.-F. Dong, J. Luo, J.-W. Li, W. Liu, G. Tan, X. Tang, J.-F. Li, J. He, and L.-D. Zhao, Science 373 (2021) 556-561.

[15] Y. Liu, M. Calcabrini, Y. Yu, S. Lee, C. Chang, J. David, T. Ghosh, M.C. Spadaro, C. Xie, O. Cojocaru-Mirédin, J. Arbiol, and M. Ibáñez, ACS Nano. (2021) DOI: 10.1021/acsnano.1c06720.

[16] X. Lou, S. Li, X. Chen, Q. Zhang, H. Deng, J. Zhang, D. Li, X. Zhang, Y. Zhang, H. Zeng, and G. Tang, ACS Nano 15 (2021) 8204-8215.

[17] Y.K. Lee, Z. Luo, S.P. Cho, M.G. Kanatzidis, and I. Chung, Joule 3 (2019) 719-731.

[18] J. Liu, P. Wang, M. Wang, R. Xu, J. Zhang, J. Liu, D. Li, N. Liang, Y. Du, and G. Chen, Nano Energy 53 (2018) 683-689.

[19] X. Shi, Z.-G. Chen, W. Liu, L. Yang, M. Hong, R. Moshwan, L. Huang, and J. Zou, Energy Storage Mater. 10 (2018) 130-138.

[20] Q. Zhang, E.K. Chere, J. Sun, F. Cao, K. Dahal, S. Chen, G. Chen, and Z. Ren, Adv. Energy Mater. 5 (2015) 1500360.

[21] A.T. Duong, V.Q. Nguyen, G. Duvjir, V.T. Duong, S. Kwon, J.Y. Song, J.K. Lee, J.E. Lee, S. Park, T. Min, J. Lee, and J. Kim, Nat. Commun. 7 (2016) 13713.

[22] J. Gainza, F. Serrano-Sánchez, M. Gharsallah, F. Carrascoso, J. Bermúdez, O.J. Dura, F.J. Mompean, N. Biskup, J.J. Meléndez, J.L. Martínez, J.A. Alonso, and N.M. Nemes, J. Appl. Phys. 126 (2019) 045105.

[23] X.L. Shi, K. Zheng, W.D. Liu, Y. Wang, Y.Z. Yang, Z.G. Chen, and J. Zou, Adv. Energy Mater. 8 (2018) 1800775.

[24] X.-L. Shi, X. Tao, J. Zou, and Z.-G. Chen, Adv. Sci. 7 (2020) 1902923.

[25] L. Su, T. Hong, D. Wang, S. Wang, B. Qin, M. Zhang, X. Gao, C. Chang, and L.-D. Zhao, Mater. Today Phys. 20 (2021) 100452.

[26] Z.H. Ge, Y. Qiu, Y.X. Chen, X. Chong, J. Feng, Z.K. Liu, and J. He, Adv. Funct. Mater. 29 (2019) 1902893.

[27] S. Li, Y. Wang, C. Chen, X. Li, W. Xue, X. Wang, Z. Zhang, F. Cao, J. Sui, and X. Liu, Adv. Sci. 5 (2018) 1800598.

[28] C. Chang, Q. Tan, Y. Pei, Y. Xiao, X. Zhang, Y.-X. Chen, L. Zheng, S. Gong, J.-F. Li, and J. He, RSC Adv. 6 (2016) 98216-98220.

[29] X.-L. Shi, W.-D. Liu, A.-Y. Wu, V.T. Nguyen, H. Gao, Q. Sun, R. Moshwan, J. Zou, and Z.-G. Chen, InfoMat 2 (2020) 1201-1215.

[30] X.-L. Shi, W.-Y. Chen, X. Tao, J. Zou, and Z.-G. Chen, Mater. Horiz. 7 (2020) 3065-3096.

[31] J. Fu, X. Su, H. Xie, Y. Yan, W. Liu, Y. You, X. Cheng, C. Uher, and X. Tang, Nano Energy 44 (2018) 53-62.

[32] F. Ren, H. Wang, P.A. Menchhofer, and J.O. Kiggans, Appl. Phys. Lett. 103 (2013) 221907.

[33] A.-Q. Xie, J. Guo, L. Zhu, and S. Chen, Chem. Eng. J. 415 (2021) 128950.

[34] H.R. Chandrasekhar, R.G. Humphreys, U. Zwick, and M. Cardona, Phys. Rev. B 15 (1977) 2177-2183.

[35] V.L. Kuznetsov, S.N. Bokova-Sirosh, S.I. Moseenkov, A.V. Ishchenko, D.V. Krasnikov, M.A. Kazakova, A.I. Romanenko, E.N. Tkachev, and E.D. Obraztsova, physica status solidi (b) 251 (2014) 2444-2450.

[36] X. Shi, A. Wu, W. Liu, R. Moshwan, Y. Wang, Z.-G. Chen, and J. Zou, ACS Nano 12 (2018) 11417-11425.

[37] X.-L. Shi, W.-Y. Chen, T. Zhang, J. Zou, and Z.-G. Chen, Energy Environ. Sci. 14 (2021) 729-764.

[38] Z. Han and A. Fina, Prog. Polym. Sci. 36 (2011) 914-944.

[39] X.L. Shi, K. Zheng, M. Hong, W.D. Liu, R. Moshwan, Y. Wang, X.-L. Qu, Z.G. Chen, and J. Zou, Chem. Sci. 9 (2018) 7376-7389.

[40] X. Shi, A. Wu, T. Feng, K. Zheng, W. Liu, Q. Sun, M. Hong, S.T. Pantelides, Z.G. Chen, and J. Zou, Adv. Energy Mater. 9 (2019) 1803242.